Coastal Engineering 116 (2016) 118–132

Contents lists available at ScienceDirect

Coastal Engineering

journal homepage: www.elsevier.com/locate/coastaleng

The California coastal wave monitoring and prediction system

W.C. O'Reilly *, Corey B. Olfe, Julianna Thomas, R.J. Seymour, R.T. Guza

Integrative Oceanography Division, Scripps Institution of Oceanography, University of California, San Diego, La Jolla, CA, United States

ARTICLE INFO

Article history:
Received 26 January 2016
Received in revised form 20 May 2016
Accepted 11 June 2016
Available online 6 July 2016

Keywords:
Ocean waves
Wave buoys
Wave models
Wave refraction
Wave runup
Longshore radiation stress

ABSTRACT

A decade-long effort to estimate nearshore (20 m depth) wave conditions based on offshore buoy observations along the California coast is described. Offshore, deep water directional wave buoys are used to initialize a non-stationary, linear, spectral refraction wave model. Model hindcasts of spectral parameters commonly used in nearshore process studies and engineering design are validated against nearshore buoy observations seaward of the surfzone. The buoy-driven wave model shows significant skill at most validation sites, but prediction errors for individual swell or sea events can be large. Model skill is high in north San Diego County, and low in the Santa Barbara Channel and along the southern Monterey Bay coast. Overall, the buoy-driven model hindcasts have relatively low bias and therefore are best suited for quantifying mean (e.g. monthly or annual) nearshore wave climate conditions rather than extreme or individual wave events. Model error correlation with the incident offshore wave energy, and between neighboring validation sites, may be useful in identifying sources of regional modeling errors.

1. Introduction

Spectral wave energy and radiation stresses, just prior to depth-limited wave breaking in the surfzone, are critical boundary conditions for modeling nearshore circulation, wave runup, and sediment transport. However, nearshore wave spectra in California often vary on relatively short longshore length scales [O(few wavelengths)] , owing to complex shelf bathymetry, making it impossible to measure directly the regional nearshore wave climate using existing measurement technology. Therefore, validated models for nearshore waves are important when managing nearshore hazards at both short and long time scales (e.g. 2 day to 50 year forecast scenarios of coastal flooding).

Nearshore waves in California are typically estimated using a Pacific ocean-scale wind-wave model (e.g. Wavewatch-III, Chawla et al., 2013) as a boundary condition for a "nested" coastal wind-wave hindcast model which resolves wavelength-scale shallow water bathymetric features (e.g. SWAN, Rogers et al., 2007; Adams et al., 2008; Van der Westhuysen et al., 2013, Barnard et al., 2014). The bias and skill of nearshore wind-wave hindcasts has improved significantly with improvements in the offshore boundary conditions (frequency-directional spectra) from the deep water wind-wave models, particularly in the swell frequency bands in the Pacific (Hanson et al., 2009). Nevertheless, challenges remain owing to the sensitivity of annual longshore wave-driven mass flux to a small bias in the nearshore wave direction parameters and the availability of historical high resolution coastal wind field boundary conditions (Rasmussen et al., 2009). Assimilating buoy measurements into wind-wave model hindcasts is an area of active research (Orzech et al., 2013; Panteleev et al., 2015), but in engineering practice nearshore buoys are mostly used for hindcast validation.

Here, in contrast to initializing a coastal wind-wave model with an ocean-scale model, a network of deep water directional buoy measurements are used to initialize a linear wave propagation model. The computationally fast model estimates nearshore wave energy and low-order directional spectra moments with O(1 wavelength) alongshore resolution. Future work combines offshore buoys and global scale models to improve the initialization of local models.

The California buoy array is described in Section 2. In Section 3, the Maximum Entropy Method (Lygre and Krogstad, 1986) is used to estimate hourly frequency-directional spectra at offshore deep water buoys, providing boundary conditions for a non-stationary linear wave propagation model (Pierson et al., 1952; Longuet-Higgins, 1957; Dorrestein, 1960; LeMehaute and Wang, 1982; O'Reilly and Guza, 1991, 1993, 1998). The spectrum is split into swell ($f = 0.0375–0.0875$ Hz) and sea ($f = 0.0875–0.5$ Hz) bands. For each nearshore prediction point, directional spectra estimates from multiple offshore buoys are combined with a weighting that depends on the frequency band, deep water wave direction and prediction buoy location (Appendix B).

In Section 4, the buoy-driven prediction methodology is validated with nearshore wave observations at 13 shallow (~20 m depth) sites. Prediction accuracy (R^2 skill, bias and rms error) is assessed for total wave energy, the centroid frequency, the peak frequency, and the mean direction.

* Corresponding author at: Integrative Oceanography Division, Center for Coastal Studies - 0209, Scripps Institution of Oceanography, University of California, San Diego, 9500 Gilman Drive, La Jolla, CA 92093-0209, United States.
E-mail addresses: woreilly@ucsd.edu (W.C. O'Reilly), colfe@ucsd.edu (C.B. Olfe), jothomas@ucsd.edu (J. Thomas), rseymour@ucsd.edu (R.J. Seymour), rguza@ucsd.edu (R.T. Guza).

http://dx.doi.org/10.1016/j.coastaleng.2016.06.005

The model performs best in the southern section of the Southern California Bight (San Clemente Basin), poorly in the Santa Barbara and San Pedro Channel regions, and moderately well elsewhere.

The potential utility of the nearshore hindcast in practical coastal engineering applications is examined in Section 5. Predictions of the longshore radiation stress, S_{xy}, the principal driver of alongshore sediment transport, validate well in north San Diego and Orange Counties for a given shore normal direction. However, uncertainty in defining the local shoreline normal creates significant S_{xy} uncertainty.

The peak frequency, f_p, a commonly used parameter in empirical wave runup formulas (Stockdon et al., 2006), is shown to be unstable in southern California when sea and swell peak energies are similar.

In Section 6, long concurrent records from southern California buoys, sheltered from incident swell by the offshore Channel Islands, are used to examine the source of model error in the swell band. At some sheltered buoys, errors correlate most strongly with conditions offshore of the Channel Islands, while errors at other buoys are more highly correlated with errors at adjacent buoys. Section 7 is a summary.

2. Wave monitoring: the California Directional Wave Buoy network

A network of 17 Waveriders at fixed deep water locations monitored incident deep water wave conditions in three relatively highly populated coastal regions; southern California (U.S. Mexico border to Morro Bay), central California (Big Sur to Bodega Bay) and northern California (Humboldt Bay Area). Six buoys were moored well offshore, seaward of islands and shoals, to monitor incident swell (squares in Fig. 1), and 11 buoys were moored near the mainland shelf break to monitor locally generated seas and validate the swell model. These observations are combined to predict sea and swell at nearshore locations along the mainland coast (Section 3). The deployment periods ranged from 5 to 14 years, all between 2001 and 2014 (Tables 1, 2).

Waveriders are translational buoys that measure accurately the sea surface position (x, y and z) of swell (O'Reilly et al., 1996). Every half-hour, on-board analysis yields estimates of the wave energy, a0, and lowest order moments of the directional wave spectrum $S(f,\theta)$ at each frequency, retained as normalized directional Fourier coefficients a1, b1, a2, and b2 (e.g., Kuik et al., 1988).

Hourly wave energy and directional Fourier coefficients are obtained by merging half-hourly records, the directional coefficients are smoothed with a 3-hour running mean filter, and a directional estimator is used to make hourly $S(f,\theta)$ wave model input spectra. Different estimators use different optimizing criteria (e.g., maximum directional smoothness, maximum entropy). The Maximum Entropy Method (MEM, Lygre and Krogstad, 1986) used here fits the measured directional coefficients exactly, eliminating any possibility of time-averaged estimator bias in the resulting directional distribution moments, compared to the original observations. MEM also produces narrow directional peaks. These are desirable estimator attributes for wave climate estimation on a swell-dominated coast.

CDIP Waverider buoy stations in shallow water, usually deployed for a few years, are used to validate the prediction methodology (Table 3).

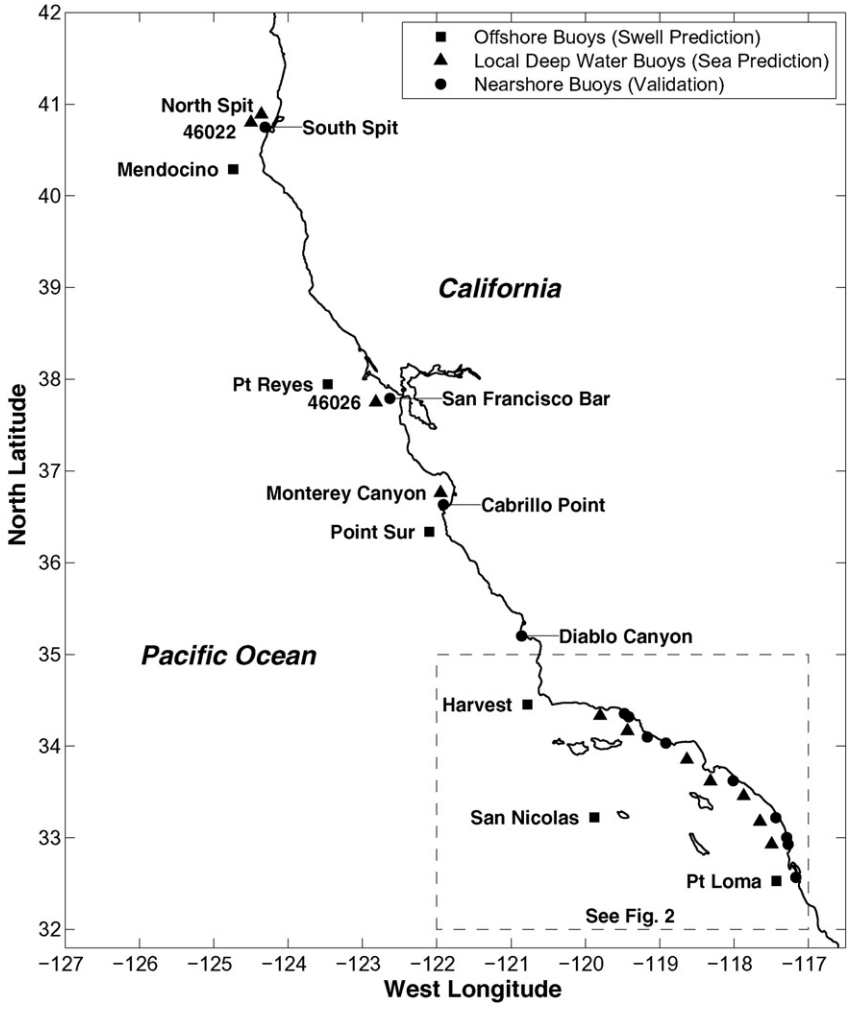

Fig. 1. Locations of buoys used to predict and validate nearshore wave parameters along the California coast. All buoys are Datawell Directional Waveriders, except 46022 and 46026 (NOAA 3 m discus buoys).

Table 1
Time periods of offshore deep water buoys (black squares, Figs. 1 and 2) used for nearshore model validation (Table 3).

Offshore station	Validation time period	Water depth (m)	Location
Cape Mendocino	06/2005–04/2013	334	40.294 N 124.740 W
Point Reyes	07/2007–06/2013	550	37.938 N 123.063 W
Point Sur	05/2009–11/2014	366	36.341 N 122.102 W
Harvest	01/2000–11/2014	548	34.458 N 120.782 W
San Nicolas Island	01/2000–11/2014	307	33.221 N 119.882 W
Point Loma South	10/2007–11/2014	1143	32.530 N 117.431 W

Most of the shallow southern California buoys are on relatively uncomplicated sandy stretches of coastline specifically selected for testing the model applicability for generic beach process studies. The few nearshore buoys in central and northern California were deployed for other applications, and severe local bathymetric features make them suboptimal for general model testing. Most of the nearshore wave predictions use Waverider observations (Fig. 1), but observations from the National Data Buoy Center (NDBC) 3 m discus buoys were sometimes used to fill data gaps, particularly for the local seas in central and northern California (e.g. 46,026 in Fig. 1). CDIP buoy stations used in this study are listed in Tables 1–3.

3. Wave prediction: a non-stationary linear spectral refraction model

A backward ray-tracing linear spectral refraction model (Pierson et al., 1952; Longuet-Higgins, 1957; and Dorrestein, 1960) is used to estimate the transformation of wave spectra from deep water buoy stations to nearshore prediction points. Spectral refraction was first used to study California swell by Munk et al. (1963), and later by LeMehaute and Wang (1982); O'Reilly and Guza (1991, 1993), and others.

Spectral refraction accounts for island blocking, wave refraction, and wave shoaling. It has been validated in Southern California (O'Reilly and Guza, 1993; O'Reilly and Guza, 1993; Rogers et al., 2002) and is well suited for the U.S. West Coast, where the continental shelf is steep and narrow, and bottom dissipation is believed small (García-Medina et al., 2013). In steady conditions, the deep water spectrum, $S_o(f,\theta_o)$, and the wave spectrum at a shallow location, $S(f,\theta)$, are related by.

$$S(f,\theta)=\frac{k(f)C_{go}(f)}{k_o(f)C_g(f)}S_o(f,\theta_o)\ \text{ where, }\ \theta_o=\Gamma(f,\theta) \tag{1}$$

The subscript, o, refers to the incident wave spectrum in deep water, k is the scalar wave number and C_g the group velocity for a given wave frequency and water depth based on the linear dispersion relation. Eq. (1) is valid along a ray path, and Γ, the relationship between θ and θ_o, is obtained by back-refracting wave rays from the shallow or sheltered site (e.g., Figs. 1–3, O'Reilly and Guza, 1991). LeMehaute and Wang (1982) refer to Γ as the inverse direction function.

Unsteady conditions are modeled by introducing time, t, and a time lag τ. Model initialization uses n deep water buoys with weighting function w.

$$\begin{aligned}S(f,\theta,t)&=\sum_{n=1}^{N}\frac{k(f)C_{go}(f)}{k_o(f)C_g(f)}S_{o,n}[f,\theta_o,t+\tau(f,\theta_o)]\cdot w(n,\theta_o);\ \ \theta_o\\&=\Gamma(f,\theta),\end{aligned} \tag{2}$$

where the time lag, $\tau(f,\theta_o)$, is estimated based on the idealized deep water path of a wave group front arriving from the direction θ_o and passing through the deep water buoys and nearshore prediction locations (Appendix B, Fig. B1). The weighting function $w(n,\theta_o)$ for buoy n is based on the proximity distance, d_n, of the buoy to the θ_o great circle path passing through the prediction site. For a given deep water direction, the more directly "upwave" or "downwave" a buoy is to the prediction site, the higher the weight relative to the other deep water buoys (see Appendix B, Fig. B1),

$$w(n,\theta_o)=\frac{d_n^{-1}}{\sum_{i=1}^{N}d_i^{-1}} \tag{3}$$

A maximum of N = 2 buoys, the highest weighted upwave and downwave buoys, are used for each θ_o arrival direction in Eq. (3). For swell prediction, $w(\theta_o)$ is also used to restrict buoy estimates of $S(\theta_o)$ to the plausible range of directions for pacific swell arrivals by setting landward directions of $w(\theta_o)=0$. Using multiple buoys for boundary conditions allows continuous nearshore predictions when some buoys are inoperable. Eq. (2) yields a linear transformation of time series of deep water directional spectra to time series of wave energy or any directional moment of the nearshore wave spectra,

$$\begin{aligned}&\int_\theta S(f,t)m_p d\theta=\\&\quad\sum_{n=1}^{N}\frac{k(f)C_{go}(f)}{k_o(f)C_g(f)}\int_\theta s_{o,n}[f,\Gamma(\mathrm{f},\theta),t+\tau(\mathrm{f},\Gamma(\mathrm{f},\theta))]w(n,\Gamma(\mathrm{f},\theta))m_p d\theta;\end{aligned} \tag{4}$$

Table 2
Time periods of local deep water buoys (black triangles, Figs. 1 and 2) used for nearshore model validation (Table 3).

Local deep water station	Validation time period	Water depth(m)	Location
NOAA 46022	06/2005–04/2013	680	40.744 N 124.575 W
North Spit	02/2010–04/2013	168	40.888 N 124.357 W
NOAA 46026	07/2007–06/2013	53	37.755 N 122.839 W
Mty. Canyon Outer	05/2009–11/2014	156	36.761 N 121.947 W
Goleta	06/2002–11/2014	182	34.333 N 119.803 W
Anacapa	06/2002–11/2014	114	34.167 N 119.435 W
Santa Monica	01/2000–11/2014	363	33.855 N 118.633 W
San Pedro	01/2000–11/2014	457	33.618 N 118.317 W
Dana Point	07/2000–11/2014	370	33.458 N 117.767 W
Oceanside	09/2005–11/2014	220	33.179 N 117.471 W
Torrey Pines	01/2001–11/2014	549	32.930 N 117.392 W

Table 3
Time periods of nearshore buoy validations (black circles, Figs. 1 and 2).

Nearshore station	Validation time period	Water depth(m)	Location
South Spit	06/2005–04/2013	40	40.753 N 124.313 W
San Francisco Bar	07/2007–06/2013	15	37.787 N 122.634 W
Cabrillo Point	05/2009–11/2014	18	36.626 N 121.907 W
Diablo Canyon	01/2000–11/2014	23	35.204 N 120.859 W
Rincon Point	09/2005–04/2007	21	34.356 N 119.475 W
Pitas Point	10/2004–09/2005	20	34.317 N 119.417 W
Port Hueneme	04/2007–02/2009	20	34.100 N 119.167 W
Leo Carillo	04/2003–03/2004	20	34.033 N 118.917 W
Huntington Beach	06/2005–11/2006	22	33.623 N 118.012 W
Camp Pendleton	01/2008–11/2014	20	33.220 N 117.439 W
San Elijo	04/2009–06/2012	20	33.003 N 117.292 W
Torrey Pines Inner	04/2001–03/2004	20	32.929 N 117.273 W
Imperial Beach	12/2006–01/2010	18	32.569 N 117.169 W

$p = 1,2,3,4,5$ where $m_1(\theta) = 1, m_2(\theta) = \cos\theta, m_3(\theta) = \sin\theta, m_4(\theta) = \cos 2\theta, m_5(\theta) = \sin 2\theta, \ldots$Eq. (4) is piece-wise integrated for discrete bandwidths of θ_o, where $\theta_o = \Gamma(f,\theta)$, to derive a linear system of equations for the transformation of discrete deep water spectra to nearshore energy and directional moments (O'Reilly and Guza, 1998),

$$\boldsymbol{b} = \mathbf{A} \cdot \boldsymbol{S_o} \tag{5}$$

The matrix $\boldsymbol{b}$ of total wave energy and directional moments at a sheltered site is related to the energy in discrete frequency-direction bins ($\Delta f, \Delta\theta_o$) of the offshore spectra, $\boldsymbol{S_o}$, by a forward model transformation matrix **A**. Each element of **A** is derived from the right-hand side of Eq. (5), which is integrated over discrete segments of the inverse direction function $\Gamma(f,\theta)$ that fall within the range of each $\Delta\theta_o$ deep water direction band.

To predict the nearshore wave spectrum using deep water buoys, the spectrum is split into swell (f = 0.0375–0.0875 Hz) and sea (f = 0.0875–0.5 Hz) components. The swell component (also known as ground swell) has distant sources, and offshore boundary conditions are applied seawards of islands and shoals (black squares, Figs 1 and 2). The sea components (also known as wind swell, chop, and local seas), generated closer to the coastline, are predicted using buoys nearer the coast, but still in deep water for waves in this frequency range (black triangles, Figs 1 and 2). The 0.0875 Hz cutoff between the sea and swell bands is based on the sharp decrease in observed swell energy at 0.08–0.10 Hz in the dispersive arrivals of swell from distant storms (e.g. Munk et al., 1963).

4. Model validation

An important purpose of the buoy network is to provide wave input to nearshore coastal process models (surfzone circulation, runup, and sediment transport). Therefore, the validation parameters are based on the aspects of nearshore waves important to nearshore processes: wave energy (E), the first moment (the centroid, f_c) of the frequency spectrum, and the mean direction of second moment of the directional spectrum ($\overline{\theta}_2$) (critical to estimating wave radiation stresses). Two additional common validation parameters, significant wave height (H_s) and the peak wave frequency (f_p), are also presented (Appendix A).

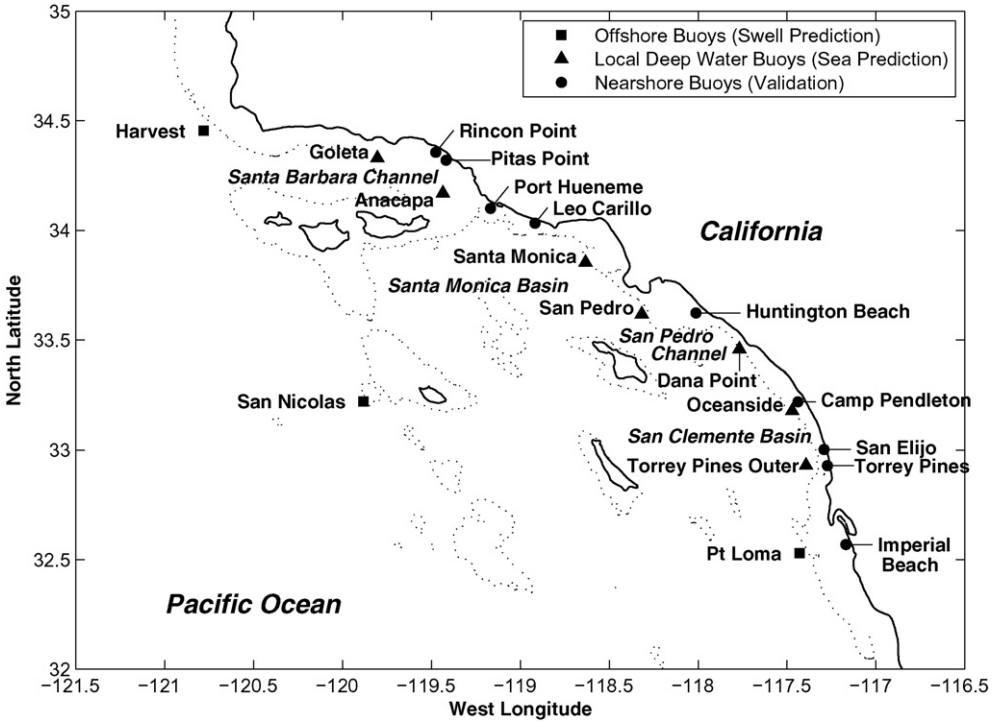

Fig. 2. Locations of buoys used to predict and validate nearshore wave parameters in the Southern California (shaded line is the 300 m depth contour). All buoys are Datawell Directional Waveriders.

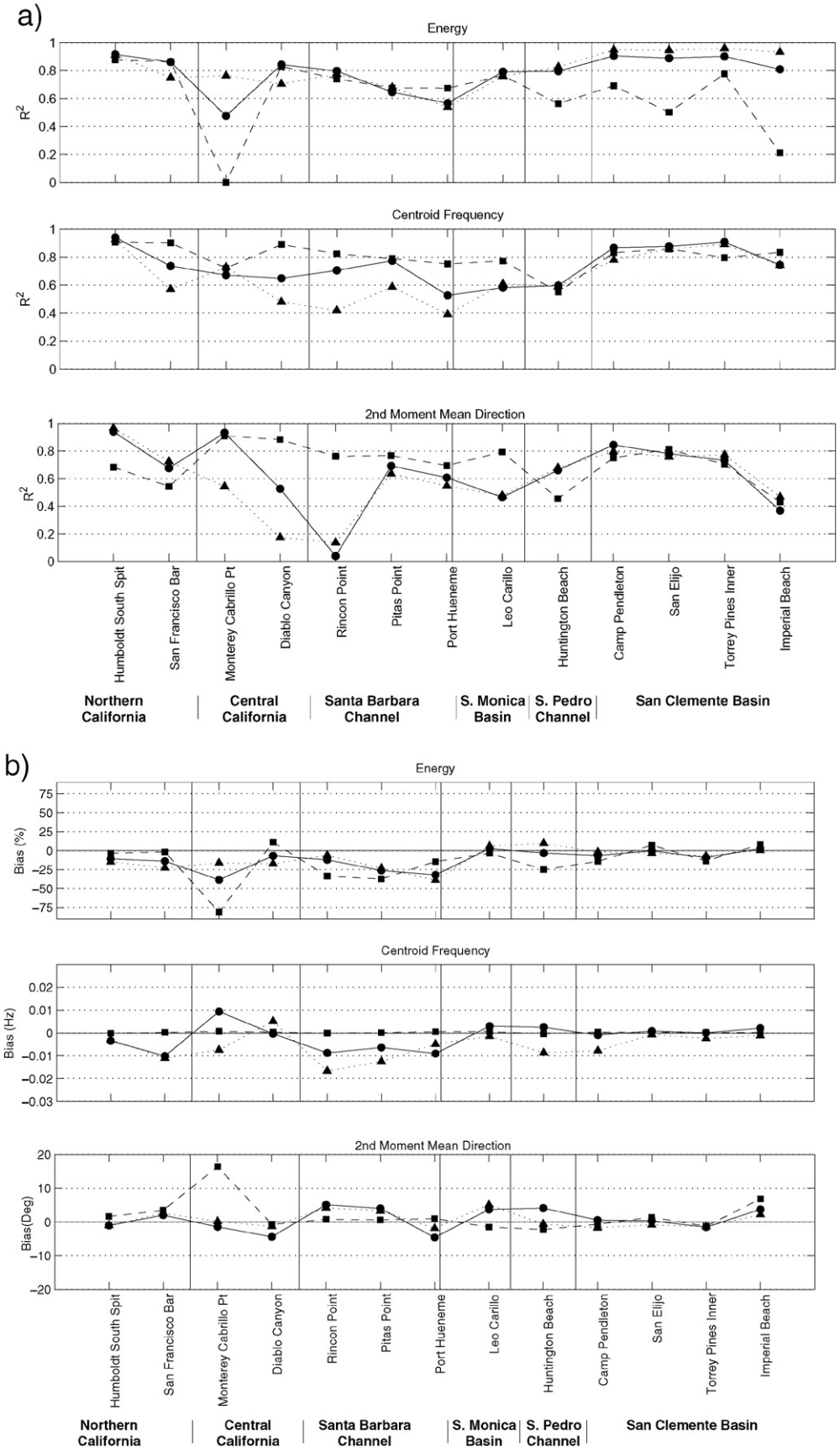

Fig. 3. Model R^2 prediction skill (a.) and bias (b.) for energy (top panels), centroid frequency (middle panels), and the bulk 2nd moment mean direction (bottom panels) at all the California nearshore validation buoys (north to south), for swell (squares), seas (triangles), and the combined total spectrum(circles).

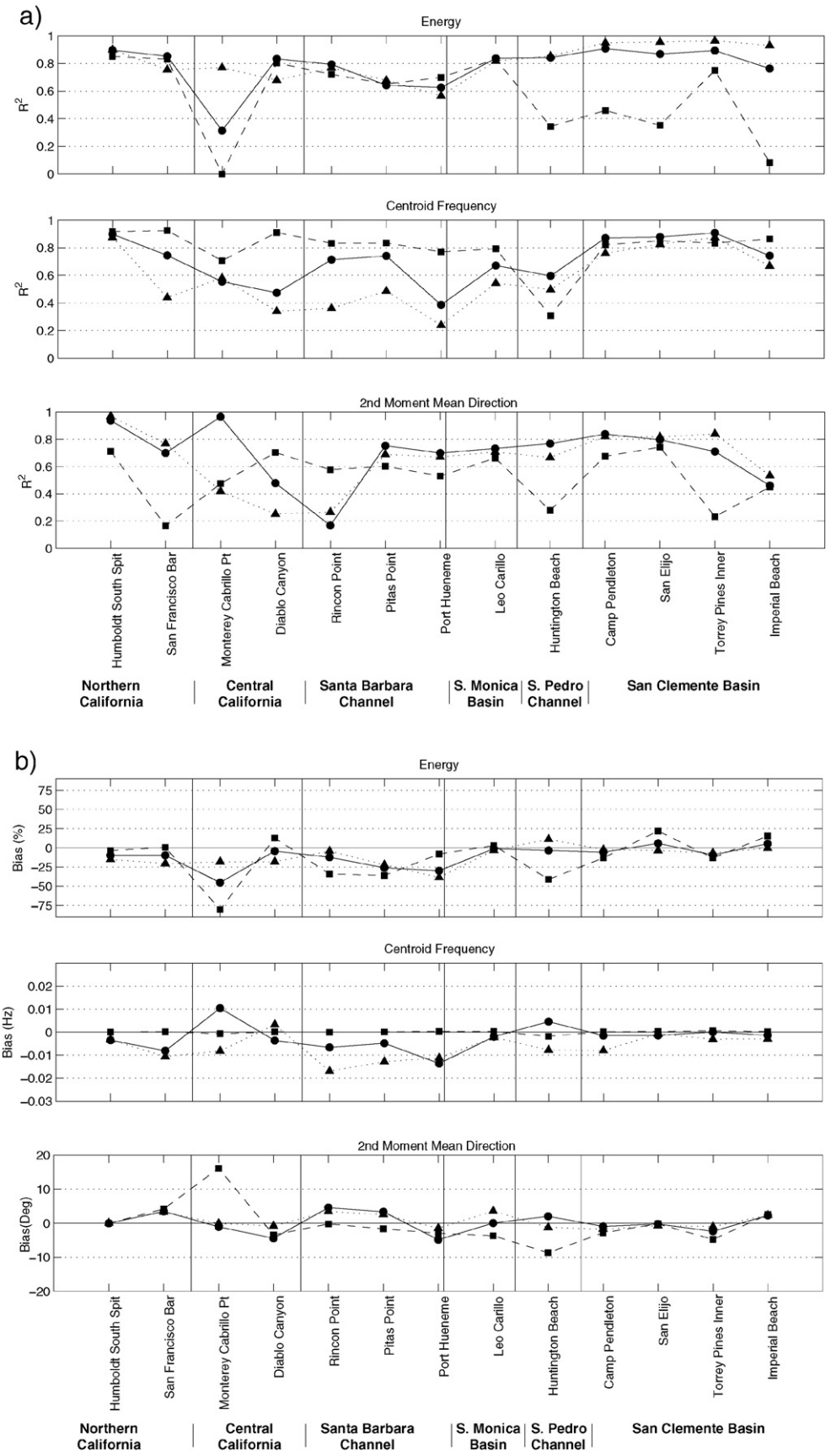

Fig. 4. a. Winter months (October–March) model R^2 prediction skill (a.) and bias (b.) for energy (top panels), centroid frequency (middle panels), and the bulk 2nd moment mean direction (bottom panels) at all the California nearshore validation buoys (north to south), for swell (squares), seas (triangles), and the combined total spectrum (circles).

However, in California, the observed and modeled f_p is sometimes unstable, jumping between sea and swell peaks of similar energy (Section 5.2).

Frequency integrated, predictions of bulk wave parameters are, from Eq. (5),

$$\begin{aligned} E(t) &= \int_f \int_\theta S(f,t)d\theta df, \\ f_c(t) &= \int_f \int_\theta f \cdot S(f,t)d\theta df \Big/ \int_f \int_\theta S(f,t)d\theta df \ , \\ \overline{\theta}_2(t) &= \frac{1}{2} arctan\left[\int\int_{f,\theta} S(f,t)\, sin2\theta d\theta df \Big/ \int\int_{f,\theta} S(f,t)\, cos2\theta d\theta df\right], \end{aligned} \tag{6}$$

where f is integrated over the swell bands, sea bands, or all frequencies. Hourly predictions (Eqs. (3) and (4)) are compared with concurrent hourly nearshore buoy observations. Model performance is assessed with: the R-squared coefficient of determination, or model skill,

$$\begin{aligned} R^2 &= 1 - \sum (pred-obs)^2 \Big/ \sum \left(obs-\overline{obs}\right)^2 \\ \text{bias} &= \frac{1}{N}\sum_1^N (pred-obs) \\ &\text{and bias removed root-mean-square errors} \\ \text{RMSE} &= \sqrt{\frac{1}{N-1}\sum_1^N (pred-obs-bias)^2} \end{aligned} \tag{7}$$

Annual model skill and bias at the nearshore buoys (Figs. 1 and 2, Table 3) are summarized in Fig. 3 (Appendix A has tabulated values), and shown seasonally (winter vs. summer months) in Figs. 4 and 5. For the year-round, total spectrum energy hindcasts (black circles, upper panel, Fig. 3a, b), the buoy-driven model shows the best nearshore hindcast skill in the San Clemente Basin section of southern California ($R^2 > 0.9$; bias < 10%). Skill is lower ($R^2 < 0.8$) and bias higher (>15%) on the south shore of Monterey Bay, and at the east end of the Santa Barbara Channel. Elsewhere, skill and bias are moderate ($0.8 < R^2 < 0.9$; bias < 15%). Centroid frequency and 2nd moment mean direction hindcasts showed similar regional performance patterns (black circles, middle and bottom panels, Fig. 3a, b), but with lower average skills than energy. R^2 can be a negative number, when the bias error exceeds the standard deviation of the observations, and is plotted as zero skill (e.g. Monterey Cabrillo Point swell skill, Fig 3a).

When decomposed into sea and swell components (black triangles and squares, Fig. 3a, b), the model performance becomes more nuanced for the San Clemente Basin nearshore sites. Swell predictions remain unbiased, but swell energy prediction skill is relatively poor ($0.4 < R^2 < 0.8$, black squares, upper panel, Fig. 3a). The total spectrum skill is high owing to the very high skills for seas (black triangles, upper panel far right, Fig. 3a). Further decomposed into seasons, San Clemente Basin swell energy skill is particularly low in winter (black squares, upper panels, Figs. 4a and 5a), with $R^2 \approx 0.25$ at Imperial Beach. The shelf bathymetry to the south of the Imperial Beach area is of lower quality than elsewhere, and is believed partially responsible for the low summer R^2. Results are improved (not shown) using alternative bathymetry from undocumented sources.

For seas, the centroid frequency, f_c, hindcast skill is poor and biased low throughout California, with the exception of the San Clemente Basin (black triangles, middle panels, Fig. 3a, b), and the 2nd moment mean direction of the local seas is poorly hindcast in central California (bottom panel, Fig. 3a, b). The lowest f_c skill is in winter, while the sea 2nd moment mean direction skill is lowest in summer (Figs. 4a and 5a).

5. Coastal engineering applications

The buoy-driven model provides relatively unbiased yearly estimates of the important nearshore spectral wave parameters, for example along the San Clemente Basin mainland coast (black dots, right-hand side of panels in Fig. 3b). Here, buoy-driven regional model hindcasts of longshore sediment transport and wave runup are compared with estimates using a nearshore buoy.

5.1. Longshore transport

In coastal engineering design and regional sediment management studies, it is typically assumed that the longshore sediment volume flux, Q_y, is linearly related to the total incident wave energy, E, and the longshore wave radiation stress, S_{xy} (Seymour and Higgins, 1978; USACE, 1984),

$$Q_y \sim \sqrt{H_s} \cdot S_{xy} \sim E^{1/4} \cdot S_{xy} \tag{8}$$

The longshore radiation stress is an integral property of the second directional moment of the incident wave spectrum just prior to wave breaking,

$$S_{xy} = \frac{1}{2}\int_f \int_\theta \frac{c_g(f)}{c(f)} S(f,\theta)\sin2(\theta-\theta_n) df d\theta \tag{9}$$

where c_g and c are the wave group and phase speeds respectively.

The sine second directional moment is calculated relative to the shoreline normal, θ_n, perpendicular to the assumed parallel nearshore depth contours. The predicted S_{xy} uses the model $S(f,\theta)$ in Eq. (9) while the nearshore buoy measures the second moment (Eq. (9)) directly. Model skill, bias and root mean square errors for hourly S_{xy} predictions at five nearshore buoys, located on relatively straight sandy sections of the San Clemente Basin and San Pedro Channel mainland coast, are shown in Table 4. For each nearshore buoy site, a local estimate of θ_n (based on the orientation of the 10 m depth contour) was used in both the local buoy and regional model S_{xy}. Model skill is good ($0.8 < R^2 < 0.9$) at Huntington Beach, Camp Pendleton, and San Elijo, with poorer skill at Torrey Pines and Imperial Beach.

Alongshore sediment transport studies, particularly those associated with regional sediment management, are often concerned with monthly, seasonal, and annual time scales. Monthly mean S_{xy} (Fig. 6) agrees much better than the hourly values, consistent with the small model energy and direction bias in this region (Fig. 3b, top and bottom). At Huntington Beach, Camp Pendleton and San Elijo, the model error (difference between the solid and dashed lines) is relatively small. Additionally, the sign of the observed and modeled annual S_{xy} are not sensitive to a $\pm 5°$ θ_n rotation (errors bars in Fig. 6). In these areas, the buoy-driven nearshore S_{xy} hindcast's seasonal and annual mean "signal" is larger than the likely "noise" owing to local shore normal uncertainty.

At Torrey Pines and Imperial Beach, S_{xy} is weaker in general, the annual average (modeled and observed) can have either sign ($\pm 5°$ scatter bars, far right, Fig. 6). In these cases, shore normal estimation methods and assumptions (e.g. alongshore and time variation of θ_n) likely play a more important role in practical, long term, longshore sediment flux calculations.

5.2. Wave runup

Stockdon et al. (2006) defines the highest 2% runup exceedance elevation, R_2, as

$$R_2 = 1.1\left(0.35\beta_f (H_0 L_0)^{\frac{1}{2}} + \frac{\left[H_0 L_0\left(0.563\beta_f^2 + 0.004\right)\right]^{\frac{1}{2}}}{2}\right) \tag{10}$$

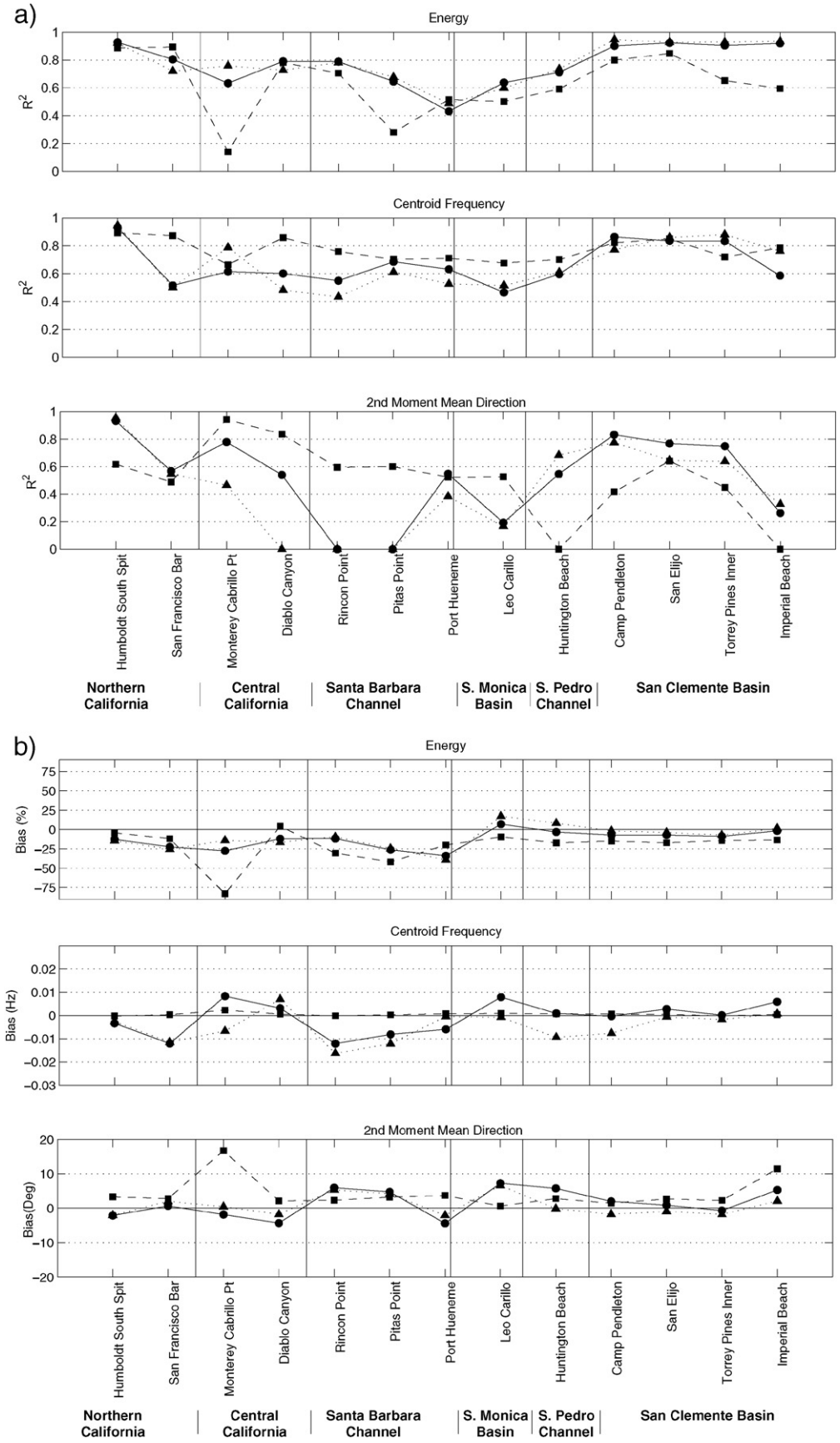

Fig. 5. a. Summer months (April–September) model R^2 prediction skill (a.) and bias (b.) for energy (top panels), centroid frequency (middle panels), and the bulk 2nd moment mean direction (bottom panels) at all the California nearshore validation buoys (north to south), for swell (squares), seas (triangles), and the combined total spectrum (circles).

where β_f is the foreshore slope, H_0 the equivalent deep water significant wave height, and L_0 the equivalent deep water wavelength based on the peak wave period, T_p, and

$$L_0 = \frac{gT_p^2}{2\pi}. \tag{11}$$

Isolating the H_0L_0 wave input parameter in Eq. (10) and replacing L_0 using Eq. (11),

$$R_2 \sim \sqrt{H_0L_0}; or \sim T_p\sqrt{H_0}; \ or \sim \frac{\sqrt{H_0}}{f_p} \tag{12}$$

where H_0 is estimated by reverse (un)shoaling the predicted nearshore significant wave height, H_s, based on the nearshore peak frequency f_p, or preferably (as done here), the predicted shallow water frequency spectrum $S(f)$ is unshoaled to deep water prior to deriving H_0 and f_p. Model predictions of hourly $\sqrt{H_0}/f_p$ at the nearshore buoys in CA are unbiased but relatively poor overall, with R^2 values <0.60 and RMSE errors exceeding 20% (Table 5).

The low R^2 skill values are largely owing to instability of the modeled and observed f_p. Although a common design wave parameter in coastal engineering practice, f_p and the corresponding peak period T_p are poor descriptors of multimodal wave frequency spectra. In California, sea and swell peaks with similar energy are common, and f_p can vary by a factor of 2–3 depending on whether the sea or swell peak is maximum (black crosses, Fig. 7), resulting in clearly nonphysical factor of 2–3 hour-to-hour fluctuations of R_2 runup. Observed f_p stability depends on the degrees of freedom (wave record length, sample rate, and frequency bandwidths) of the processed spectral data. Therefore, the model f_p predictive skill depends significantly on wave climate (e.g. presence of comparable sea and swell peaks) and data analysis factors (e.g. degrees of freedom) that are unrelated to the wave transformation model skill.

For general climatic hindcasts (e.g. estimating runup during daily high tide) at locations where multimodal sea states are common, it would desirable to use an alternative empirical wave runup equation using a more stable frequency parameter.

The centroid frequency f_c is far more stable (red circles, Fig. 7), but is heavily weighted by the high frequency (short wavelengths) tails of the spectra. A bulk frequency parameter that is more relevant to runup dynamics is the frequency of the centroidal wavelength, f_{cL} (green diamonds, Fig. 7),

$$f_{cL} = \sqrt{\frac{g}{2\pi L_{oc}}}, \tag{13}$$

with the centroidal wavelength $L_{oc} = \iint_{f,\theta} L_o(f)\cdot S(f)d\theta df / \iint_{f,\theta} L_o(f)\cdot d\theta df$, and where $S(f)$ is unshoaled to deep water.

The potential utility of f_{cL} in climatic studies is illustrated at the Camp Pendleton nearshore buoy (Fig. 8) where the bulk of the RMSE error in the hourly runup wave input parameter, and the source of the low R^2, is the "cloud" of poor predictions for the lower half of the $\sqrt{H_0}/f_p$ values. The frequency of the centroid wavelength f_{cL} is more stable, with improved R^2 (right panel in Fig. 8, skill values in brackets in Table 5). However, f_{cL} should not be used directly with the Stockdon et al. formulas, because f_p was used in their model calibration. Instead, a best fit coefficient, C_f, between the two wave input parameters, $\sqrt{H_0}/f_p = C_f\sqrt{H_0}/f_{cL}$ would have to be derived from deep water buoy data prior to using f_{cL} in Eq. 10.

Finally, the overall fit at the highest values of $\sqrt{H_0}/f_p$ (upper right corner of left panel, Fig. 8) improves because the largest incident wave frequency spectra are more unimodal, and f_p is more stable and predictable. Model predictions at most nearshore buoys (not shown) also have considerably less scatter in of the largest values of $\sqrt{H_0}/f_p$. Thus, these results do not discourage the use of f_p in Stockdon et al. (Eq. 10 above) when estimating design wave runup elevations for the most extreme wave events (a primary application of Eq. (10)).

Table 4
Nearshore validation statistics for hourly S_{xy} (validation time periods listed in Table 3).

Nearshore buoy	R^2	Mean (cm^2)	Bias (cm^2)	RMSE (cm^2)
Huntington Beach	0.82	−10	−10	39
Camp Pendleton	0.89	−21	−4	34
San Elijo	0.80	32	4	28
Torrey Pines	0.63	−20	12	35
Imperial Beach	0.34	15	−10	45

For each site, S_{xy} has been calculated relative to an estimate of the local shoreline normal. The mean values are based on the observations. The bias and root mean square errors are model errors relative to the observations. Positive S_{xy} values correspond to northward or "upcoast" directed stress.

6. Discussion

The buoy-driven modeling methodology was originally developed for use in concert with beach change studies on long, straight beaches in the San Clemente Basin region. Particular attention was given to the placement of deep water and nearshore buoys for this purpose, and this contributes to the relatively high skill in San Diego County. In contrast, nearshore validation buoys in central and northern California were deployed for other, often very site-specific purposes, in areas with locally complex or rocky shallow water bathymetry. These are demanding sites to model owing to dependence on local bathymetry or extreme sheltering. For example, while the hindcast skill at the Cabrillo Point buoy site in Monterey Bay is notably poor, with a large underprediction bias and negligible skill in the swell band, this site is highly sheltered on a northeast-facing rocky section of coast. An earlier, more time limited comparison of the buoy-driven hindcast model to wave measurements further east in Monterey Bay, on a sandy more exposed section of the coastline, yielded better results (Orzech et al., 2010).

The present model validation metrics are more stringent than are typically used to assess wind-wave hindcast model performance. In particular, S_{xy} depends on the mean direction of the incident wave energy flux relative to shore normal $\theta - \theta_n$ immediately seaward of the breakpoint. Significant wave height, a commonly used model validation metric, is better predicted than energy (tabular statistics in Appendix A) but is of lesser value in state-of-the-art nearshore process modeling. The peak wave frequency f_p, or peak period T_p, is also commonly used in wave hindcasting studies, but it is problematic for the California wave climate. Bimodal frequency spectra with similar magnitude swell and sea energy peaks are common, particularly in southern California, and using peak frequency estimates for anything other than extreme wave runup estimation is discouraged in favor of the more robust centroid frequency or wavelength.

6.1. Sources of nearshore sea hindcast errors

Local sea hindcast skill was highest in the San Clemente Basin, where the mainland shelf is particularly narrow and deep water buoys are closest to the coast (Fig. 2).

In general, the sea hindcasts skill decreased in the winter, with distance between the deep water buoys and the prediction sites, and with more north-south coastline orientations. In addition, the nearshore sea centroid frequency was consistently biased low north of the San Clemente Basin sites. This is consistent with an increased violation of underlying buoy-driven modeling assumption that the local seas were sufficiently spatially homogeneous, and the buoy close enough to the coastal site, that the local buoy spectra boundary condition could be propagated to the nearshore site without invoking a wind-wave generation model.

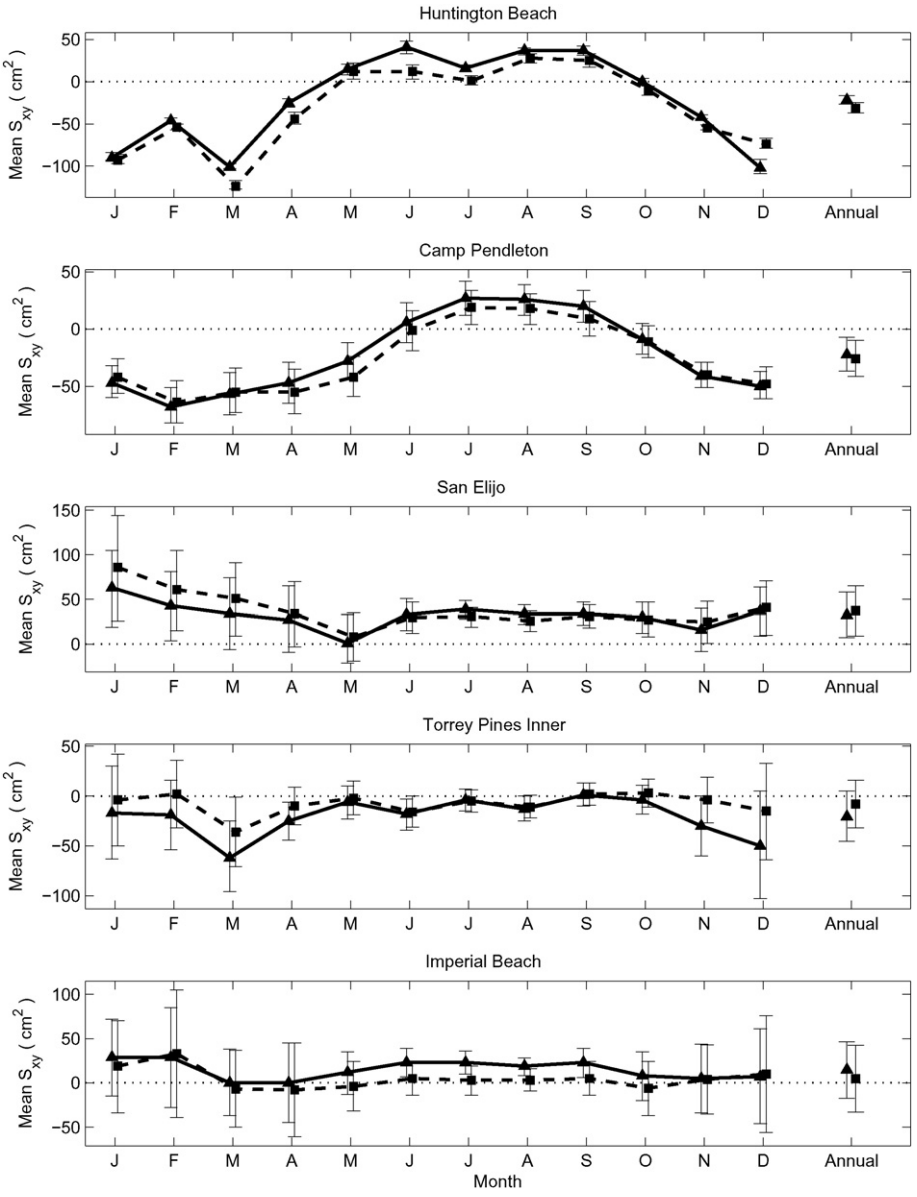

Fig. 6. Mean observed (solid line, black triangles) and predicted (dashed line, black squares) longshore radiation stress, S_{xy}, both monthly and annually (mean of month means) at five nearshore buoys in the San Pedro and San Clemente Basin regions of southern California (Fig. 2, Table 3). The errors bars represent the sensitivity of the means to a ± 5° change to the shore normal used in the S_{xy} calculations. Positive values correspond to a northward or upcoast-directed stress.

6.2. Sources of nearshore swell hindcast errors

Nearshore swell hindcasts (black squares, Figs. 3–5) typically showed lower energy skills than seas, but higher centroid frequency and 2nd moment mean direction skills. Swell in California exhibits strong seasonal behavior, with the most energetic swell arriving from the west in winter (October–March), while less energetic but persistent south swell from the southern hemisphere dominate in summer (April–September). This is believed to be the cause of the lower swell energy skill in the San Clemente Basin during winter (black squares, upper panel, Fig. 4a) when the swell must propagate through gaps between the offshore islands, compared to the higher skill summer months (black squares, upper panel, Fig. 5a) when swell arrives in the San Clemente Basin from the south with no island blocking.

Table 5
Nearshore validation statistics of the hourly 2% exceedance runup elevation input parameter $\sqrt{H_0}/f_p$.

Nearshore buoy	R^2	Bias (%)	RMSE (%)
Huntington Beach	0.34 [0.68]	−6 [−7]	21 [11]
Camp Pendleton	0.52 [0.84]	−3 [−3]	18 [8]
San Elijo	0.54 [0.85]	−1 [−1]	20 [10]
Torrey Pines	0.60 [0.90]	−4 [−3]	21 [9]
Imperial Beach	0.50 [0.83]	−2 [−2]	22 [11]

Validation time periods listed in Table 3. Validation results replacing f_p with the more statistically stable frequency of the centroidal wavelength f_{cL} are shown in the brackets.

The time lag approximation, τ (Eq. (5)) is a potential source of forward model error, but model skill R^2 was at most only marginally improved at the 13 nearshore sites by shifting $\tau \pm 4$ h relative to the buoy time series (Fig. 9). Nevertheless, skill in the sea band is improved by a −1 hour shift at many sites, while the swell band is better aligned with no shift from the model lags (as large as 7 h in the swell band). The sea band result is consistent with the local deep water buoy and nearshore buoy falling within the same local wind event fetch. The highest frequency sea energy at both buoys rise and fall together rather than the local sea propagating shoreward from the local deep water buoy

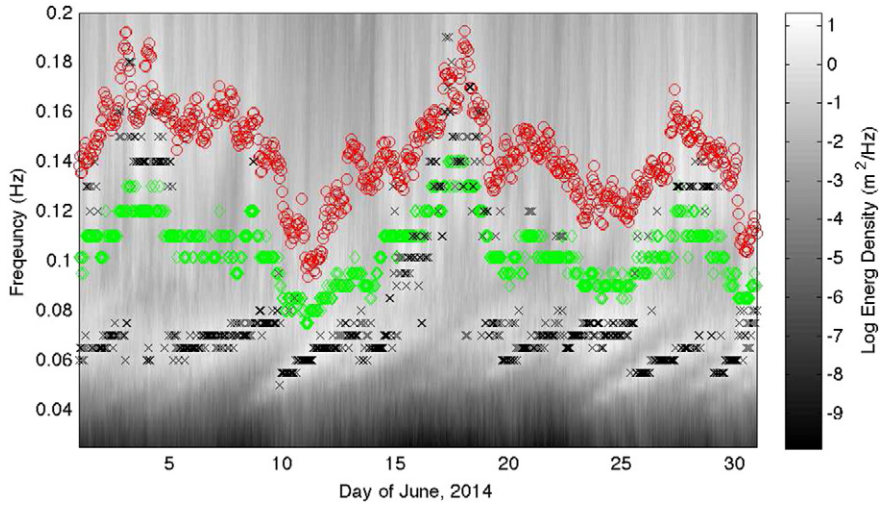

Fig. 7. Observed hourly frequency spectra from the Point Loma South buoy versus time for June 2014. When locally generated high frequency seas ($f > 0.10$ Hz) and the more consistent swells ($f < 0.10$ Hz) have similar energy, the observed hourly peak frequency f_p (black cross) is unstable, and jumps between the swell and sea bands (e.g. June 1–5, 15–20, and 27–30). In contrast, the centroidal frequency f_c (red circle) and the frequency of the centroidal wavelength, f_{cL} (green diamond) are more stable.

with the (small, but non-zero) estimated time lag. Overall, this analysis shows that R^2 is relatively insensitive to small time lag errors (R^2 curves are flat around the R^2 peaks) and using the local deep water buoy sea band information with zero time lag may be preferable for nearshore predictions in many cases.

Two primary sources of model error in the swell band are the deep water boundary condition (buoy estimates of deep water directional spectra, $\boldsymbol{S_o}$, Eq. (5)) or the forward wave model used to transform those boundary conditions to the nearshore sites ($\mathbf{A}$, Eq. (5)). Isolating these errors is not straightforward. The spatial correlation of wave model errors between adjacent validation sites, and between each validation site and the offshore wave energy, provides preliminary suggestions.

First it is assumed that the offshore boundary condition errors are mostly random in each offshore direction bin. The Datawell MK-I/II/III series of buoys have been shown to accurately measure basic swell parameters in California (O'Reilly et al., 1996). Noise levels are relatively low. Directional estimators, like the MEM estimator used here, are surprisingly robust for many practical applications. Nevertheless, all buoys commonly used today are fundamentally low resolution directional instruments (Ochoa and Gonzalez, 1990). The limited (typically 1 h) observation time of buoy estimates also imposes fundamental (e.g. statistical) limitations on the accuracy of input deep water boundary conditions to the model. Directionally symmetric unimodal directional distributions (e.g. a solo swell arrival from a distant, slow moving storm) are the best case scenario for estimator performance. The directional sea-state at any given wave frequency depends on the number of concurrent wave events and their directional symmetry, but is unlikely to be a strong function of wave energy. Therefore, if deep water directional estimates are a significant source of error, and those errors are randomly distributed over the offshore directions (e.g. resulting from statistical uncertainty in the buoy measurements of the low order moments), then one would *not expect* the nearshore errors to be correlated with the deep water wave energy, but instead with the (unknown) true complexity of offshore directional-sea-state.

On the other hand, forward model errors, which manifest themselves in the (fixed) linear transformation matrix described by the

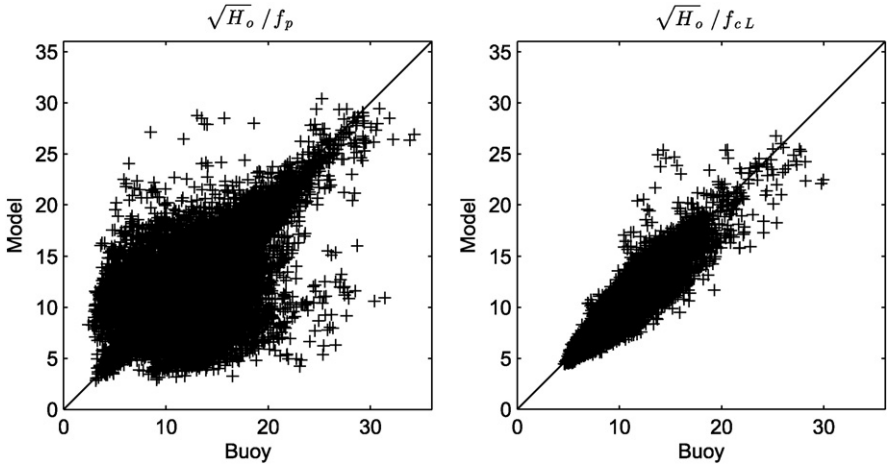

Fig. 8. At the Camp Pendleton nearshore buoy, hourly model predictions versus observations, of (left panel) the peak frequency-dependent Stockdon et al. (2006) highest 2% runup exceedance wave input parameter, $\sqrt{H_0}/f_p$, and (right panel) the more statistically robust centroid wavelength frequency-dependent parameter, $\sqrt{H_0}/f_{cL}$. Buoy and model estimates of the nearshore frequency spectrum were reverse shoaled to deep water prior to calculating H_0, f_p and f_{cL}.

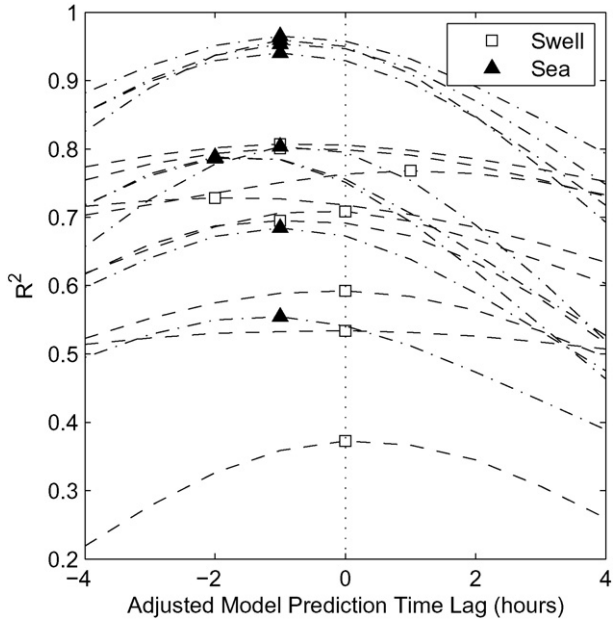

Fig. 9. Model skill R^2 as a function of adjusted model prediction time lag correction. The maximum R^2 (symbols) are at small lags, and corrections to R^2 are small.

right-hand side of Eq. (5), should lead to a correlation between deep water energy and nearshore errors (assuming correct deep water directional distributions). Forward model errors can occur for a host of reasons, most notably missing physics (e.g. diffraction, reflection, wind generation, bottom attenuation, currents, tide elevation changes, nonlinear interactions) or inaccurate shelf bathymetry leading to errors in the inverse direction function, Γ.

The issue of model error correlation is explored with additional swell band validation at the seven local deep water buoys in southern California (black triangles, Fig. 2, and Table 2). These buoys are inside the islands at the edge of the mainland shelf and are heavily sheltered from swell by the islands like the nearshore buoys. However, they have all been deployed and maintained continuously by CDIP since June 2002, and provide a unique set of 91,591 h of concurrent swell model error time series.

Model performance for swell at the local deep water buoys was found to be similar to the nearshore buoy results, with large negative energy bias in the two Channels (Goleta, Anacapa, San Pedro buoys), and moderate agreement everywhere else (Table 6). Moderate negative error correlation was found between the buoys in the Channels, which is consistent with the swell underprediction errors increasing with higher offshore wave energy, suggesting that the forward model errors may be significant in these areas.

Table 6
Local deep water buoy swell validation statistics and error correlations.

Local deep water buoy	Swell spectrum energy f = 0.04 – 0.0975Hz			Error corr. w/ offshore swell energy
	R^2	Bias	RMSE	r
Goleta	0.70	−38%	93%	**−0.52**
Anacapa	0.50	−41%	89%	**−0.55**
Santa Monica	0.78	−8%	52%	0.18
San Pedro	0.70	−30%	81%	**−0.27**
Dana Point	0.70	−13%	47%	0.03
Oceanside	0.64	−11%	48%	0.12
Torrey Pines Outer	0.80	−6%	42%	0.19

Table 7
Local deep water buoy-buoy swell model error correlations.

	San Clemente Basin		San Pedro Channel		Santa Monica Basin	S. Barbara Channel	
	Torrey Pines	Oceanside	Dana Point	San Pedro	Santa Monica	Anacapa	Goleta
Goleta	−0.15	0.09	0.10	**0.48**	0.11	**0.33**	1.0
Anacapa	−0.03	0.05	0.16	**0.31**	−0.01	1.0	
Santa Monica	0.20	**0.40**	0.22	**0.33**	1.0		
San Pedro	0.09	**0.41**	**0.34**	1.0			
Dana Point	**0.31**	**0.30**	1.0				
Oceanside	**0.35**	1.0					
Torrey Pines	1.0						

Very little correlation was found between model errors and offshore swell energy at the other buoy locations, implying that errors in the remainder of the Bight are primarily owing to offshore boundary condition errors.

The concurrent local deep water buoy error time series allow for an additional analysis of the spatial correlation of errors between the different buoys (Table 7).

While the spatial error correlation coefficients between the buoys are generally low, it is notable that the correlations are all positive, showing a tendency for Bight-wide over- or underprediction at any given time. In addition, the spatial correlations between the "non-Channel" buoys are consistently higher than their individual correlations with offshore energy (shaded cells, Table 6 vs. Table 7), further suggesting that model errors outside the Channels are dominated by offshore boundary condition errors.

The San Pedro buoy error results appear to straddle the fence between boundary condition and forward model errors, showing a correlation with offshore energy and spatial correlation with the Goleta, Anacapa, Dana Point and Oceanside buoys. Model errors in the San Pedro area are likely a more balanced mix of offshore boundary condition and forward model errors.

7. Summary

A method to predict nearshore waves by combining multiple deep water buoy observations with a numerical wave propagation model is presented. Model performance metrics, based on wave parameters for regional sediment management and skillful nearshore process modeling, are used to assess model performance.

The regional, buoy-driven methodology demonstrated high skill and low bias in the San Clemente Basin of southern California, where the buoy-driven nearshore hindcast resolves the strength and direction of the longshore wave radiation stress on monthly, seasonal and annual time scales. At other locations, neither the model nor the observations convincingly demonstrate even the sign of annual alongshore sediment transport.

Even at the best validation sites, detailed hourly predictions showed significant weaknesses when parsed seasonally, into individual events, or into sea and swell components. The hourly nearshore hindcast skill was particularly poor in the Santa Barbara Channel and along the highly sheltered southern coast of Monterey Bay. Based on the temporal correlation of model errors with offshore swell energy, and the spatial correlation of model errors within geographic regions, it is hypothesized that the winter swell errors in the

San Clemente Basin are primarily owing to uncertainty in the shape of the offshore swell directional spectra (offshore boundary condition errors), while the errors in the Santa Barbara Channel are primarily the result of missing model physics (wave transformation errors).

The nearshore wave observations available for hindcast validation are limited, but provide a context for future modeling testing and improvement. Crosby et al. (in press) shows that some of the sites poorly modeled here (e.g. Santa Barbara Channel) are also modeled poorly by an operational wind-wave generation and propagation model (WW3). A better understanding of wave spectra evolution in these regions may require new site-specific observations and modeling methods. This work highlights the importance of making nearshore validation observations along populated stretches of California coastline where high quality wave model hindcasts are critical to the success of future coastal management and science studies.

Acknowledgements

This study and the CDIP California wave buoy network were cooperatively funded by the California Department of Parks and Recreation, Division of Boating and Waterways Oceanography Program, and the United States Army Corps of Engineers.

Additional wave buoy support was provided by the U.S. Navy (San Nicolas Island and Camp Pendleton buoys,) Pacific Gas and Electric (Diablo Canyon buoy) and the Stanford University Hopkins Marine Lab (Cabrillo Point buoy). The supplemental NOAA buoy data used in the study was provided by the NOAA National Data Buoy Center (NDBC).

The 14 year dataset of wave observations from the CDIP wave monitoring network is unique in its size (17 stations), data continuity and accuracy (Datawell MK series Waverider buoys used throughout), and completeness (few data gaps of more than a week or two). For this, we thank the talented and dedicated staff of CDIP.

Appendix A. Nearshore buoy validation tables

Table A1
Northern and central California nearshore buoy validation statistics (Fig. 1, Table 3).

Nearshore buoy (hourly records)	Bulk val	Total spectrum f = 0.04 − 0.50 Hz			Swell spectrum f = 0.04 − 0.0975 Hz			Sea spectrum f = 0.0975 − 0.50 Hz		
		R^2	Bias	RMSE	R^2	Bias	RMSE	R^2	Bias	RMSE
South Spit, Eureka (78,835)	E	0.92	−11%	25%	0.88	−4%	61%	0.91	−15%	16%
	f_c	0.94	−3%	4%	0.91	<−1%	2%	0.93	−2%	3
	$\overline{\theta}_2$	0.94	−1°	5°	0.68	2°	11°	0.97	<−1°	2°
	H_s	0.94	−6%	9%	0.94	−2%	21%	0.94	−7%	6%
	f_p	0.75	−1%	14%	0.57	<−1%	9%	0.79	<1%	9%
San Francisco Bar (42,844)	E	0.86	−14%	36%	0.86	−2%	63%	0.75	−23%	36%
	f_c	0.74	−7%	11%	0.90	<1%	2%	0.57	−7%	10%
	$\overline{\theta}_2$	0.68	2°	8°	0.54	3°	10°	0.72	3°	8°
	H_s	0.89	−8%	13%	0.94	−2%	19%	0.78	−13%	15%
	f_p	0.43	−1%	24%	0.59	<−1%	9%	0.44	<−1%	19%
Cabrillo Point, Monterey Bay (49,804)	E	0.48	−38%	56%	< 0	−81%	116%	0.76	−16%	46%
	f_c	0.67	7%	13%	0.72	1%	4%	0.73	−5%	11%
	$\overline{\theta}_2$	0.93	−1°	4°	0.91	16°	5°	0.54	<1°	1°
	H_s	0.54	−20%	23%	< 0	−59%	39%	0.81	−7%	19%
	f_p	<0	18%	28%	0.30	−1%	11%	0.36	−7%	20%
Diablo Canyon, San Luis Obispo (128,072)	E	0.84	−7%	34%	0.83	11%	62%	0.70	−17%	38%
	f_c	0.65	<−1%	12%	0.89	<1%	2%	0.48	3%	10%
	$\overline{\theta}_2$	0.53	−4°	9°	0.88	−1°	8°	0.17	−1°	15°
	H_s	0.84	−4%	15%	0.91	4%	19%	0.56	−10%	22%
	f_p	0.31	−3%	25%	0.53	<−1%	10%	0.07	<−1%	22%

Table A2
Santa Barbara Channel and Santa Monica Basin nearshore buoy validation statistics (Fig. 2, Table 3).

Nearshore buoy (no. hourly records)	Bulk val	Total spectrum f = 0.04 − 0.50 Hz			Swell spectrum f = 0.04 − 0.0975 Hz			Sea spectrum f = 0.0975 − 0.50 Hz		
		R^2	Bias	RMSE	R^2	Bias	RMSE	R^2	Bias	RMSE
Rincon Point, Santa Barbara Chan. (14,063)	E	0.80	−12%	36%	0.74	−34%	83%	0.77	−6%	38%
	f_c	0.71	−5%	10%	0.82	<−1%	3%	0.42	−9%	9%
	$\overline{\theta}_2$	0.04	5°	8°	0.76	1°	6°	0.14	4°	9°
	H_s	0.82	−6%	15%	0.76	−20%	27%	0.83	−3%	15%
	f_p	0.34	6%	35%	0.32	−1%	11%	0.40	−1%	27%
Pitas Point, Santa Barbara Chan. (7874)	E	0.65	−26%	39%	0.68	−37%	72%	0.68	−23%	44%
	f_c	0.77	−4%	10%	0.79	<1%	3%	0.59	−7%	9%
	$\overline{\theta}_2$	0.69	4°	9°	0.77	1°	7°	0.64	3°	11°
	H_s	0.70	−14%	15%	0.66	−23%	25%	0.75	−12%	17%
	f_p	0.36	3%	35%	0.30	−1%	11%	0.42	−1%	27%
Port Hueneme, Santa Barbara Chan. (13,962)	E	0.57	−32%	50%	0.67	−14%	71%	0.54	−39%	63%
	f_c	0.53	−6%	14%	0.75	<1%	3%	0.39	−2%	13%
	$\overline{\theta}_2$	0.61	−5°	18°	0.70	1°	11°	0.55	−2°	13°
	H_s	0.56	−16%	18%	0.63	−8%	23%	0.58	−21%	21%

Table A2 (*continued*)

Nearshore buoy (no. hourly records)	Bulk val	Total spectrum f = 0.04 − 0.50 Hz			Swell spectrum f = 0.04 − 0.0975 Hz			Sea spectrum f = 0.0975 − 0.50 Hz		
		R^2	Bias	RMSE	R^2	Bias	RMSE	R^2	Bias	RMSE
	f_p	0.23	−6%	39%	0.37	<−1%	10%	0.25	−3%	34%
Leo Carillo, Santa Monica Basin (8141)	E	0.79	3%	33%	0.76	−3%	39%	0.76	6%	45%
	f_c	0.58	2%	13%	0.77	1%	3%	0.61	−1%	10%
	$\bar{\theta}_2$	0.47	4°	12°	0.79	−2°	5°	0.48	5°	9°
	H_s	0.77	1%	14%	0.73	−3%	17%	0.74	3%	20%
	f_p	<0	3%	36%	0.33	<1%	10%	0.18	−1%	33%

Table A3
San Pedro Channel and San Clemente Basin nearshore buoy validation statistics (Fig. 2, Table 3).

Nearshore buoy (no. hourly records)	Bulk val	Total spectrum f = 0.04 − 0.50 Hz			Swell spectrum f = 0.04 − 0.0975 Hz			Sea spectrum f = 0.0975 − 0.50 Hz		
		R^2	Bias	RMSE	R^2	Bias	RMSE	R^2	Bias	RMSE
Huntington Bch, San Pedro Channel (12,356)	E	0.80	−3%	30%	0.56	−25%	50%	0.83	10%	38%
	f_c	0.60	2%	16%	0.55	−1%	4%	0.59	−4%	13%
	$\bar{\theta}_2$	0.66	4°	19°	0.46	−2°	12°	0.68	−1°	14°
	H_s	0.78	−2%	13%	0.56	−15%	21%	0.81	4%	16%
	f_p	0.05	7%	35%	0.15	−2%	12%	0.15	<1%	36%
Camp Pendleton, San Clemente Basin (58,570)	E	0.91	−6%	27%	0.69	−14%	46%	0.95	−2%	28%
	f_c	0.87	−1%	8%	0.83	1%	3%	0.78	−4%	6%
	$\bar{\theta}_2$	0.84	1°	6°	0.75	−1°	5°	0.80	−2°	7°
	H_s	0.91	−3%	10%	0.78	−8%	15%	0.95	−1%	10%
	f_p	0.41	2%	27%	0.41	<1%	12%	0.39	−5%	26%
San Elijo, San Clemente Basin (28,688)	E	0.89	<1%	34%	0.50	7%	87%	0.95	−4%	28%
	f_c	0.88	1%	7%	0.86	1%	2%	0.86	< 1%	6%
	$\bar{\theta}_2$	0.78	<1°	5°	0.81	1°	5°	0.76	−1°	5°
	H_s	0.90	−1%	13%	0.79	−1%	23%	0.94	−2%	12%
	f_p	0.42	<1%	29%	0.43	<1%	10%	0.56	−2%	21%
Torrey Pines, San Clemente Basin (24,991)	E	0.90	−9%	32%	0.78	−13%	80%	0.96	−7%	21%
	f_c	0.91	<1%	7%	0.80	<1%	3%	0.89	−1%	5%
	$\bar{\theta}_2$	0.73	−2°	4°	0.70	−1°	6°	0.77	−1°	4°
	H_s	0.92	−5%	10%	0.87	−7%	21%	0.96	−4%	8%
	f_p	0.49	<1%	29%	0.34	<1%	10%	0.55	−4%	22%
Imperial Beach, San Clemente Basin (26,412)	E	0.81	3%	44%	0.21	8%	123%	0.93	<1%	30%
	f_c	0.74	1%	10%	0.83	<1%	3%	0.74	−1%	8%
	$\bar{\theta}_2$	0.37	4°	6°	0.43	8°	8°	0.47	2°	6°
	H_s	0.90	<1%	13%	0.77	−2%	25%	0.94	<1%	11%
	f_p	0.27	3%	32%	0.36	<1%	11%	0.43	<1%	23%

Appendix B. Time lag estimation and multi-buoy weighting

The wave energy time lag between a buoy and a prediction site, τ, is based on the shortest direct deep water path, or lag distance, d_L, and the deep water group velocity, C_{go}. Increased lag time owing to wave refraction and shoaling is assumed to be small relative to the 1 hour model time step.

$$\tau(f,\theta_o) = d_L \cdot C_{go}(f) \tag{B1}$$

The lag distance (in arc degrees) is a function of the great circle distance between the buoy and prediction site, d_B, and the incident deep water direction, θ_o, (either true compass "arriving from" or "headed to" direction is ok)

$$d_L = d_B \cdot \cos(\theta_o - \beta) \tag{B2}$$

where β is the true compass heading from the buoy to the prediction site. Both $d_B$and β are derived using great circle equations,

$$d_B = \arccos\left[\sin(\varphi_B)\sin\left(\varphi_p\right) + \cos(\varphi_B)\cos\left(\varphi_p\right)\cdot\cos(\lambda_P - \lambda_B)\right] \tag{B3}$$

$$\beta = \arctan\frac{\cos(\varphi_p)\cdot\sin(\lambda_P - \lambda_B)}{\cos(\varphi_B)\sin(\varphi_P) - \sin(\varphi_B)\cos(\varphi_P)} \quad . \tag{B4}$$

The "upwave" (shown in B.1) or "downwave" direct path proximity distance for buoy "n" (d_n), for a given prediction site, is

$$d_n = d_B \cdot |\sin(\theta_o - \beta)| \tag{B5}$$

and is used to weight the deep water directional spectrum boundary condition, $S_o(\theta)$, for $\theta = \theta_o$ as,

$$w(n,\theta_o) = \frac{d_n^{-1}}{\sum_{i=1}^{N} d_i^{-1}} \tag{B6}$$

where N is the total number of deep water buoys being used to estimate $S_o(\theta)$. Best results were obtained by restricting N to a maximum of 2 for each θ_o, representing the most proximal upwave buoy and (if it exists) downwave buoy for each incident deep water wave direction.

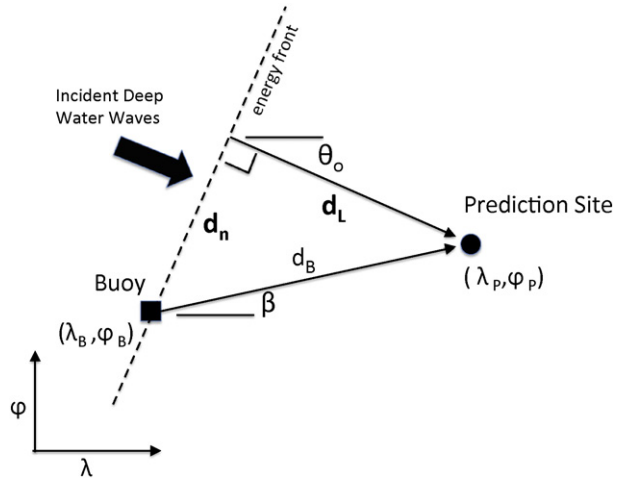

Fig. B1. Schematic of a buoy's direct path time lag distance ($\mathbf{d_L}$) and direct path proximity distance ($\mathbf{d_n}$) calculation based on the incident deep water wave direction θ_o.

References

Adams, P.N., Inman, D.L., Graham, N.E., 2008. Southern California deep-water wave climate: characterization and application to coastal processes. J. Coast. Res. 24 (4), 1022–1035.

Barnard, P.L., van Ormondt, M., Erikson, L.H., Eshleman, J., Hapke, C., Ruggiero, P., Adams, P.N., Foxgrover, A.C., 2014. Development of the coastal storm modeling system (CoSMoS) for predicting the impact of storms on high-energy, active-margin coasts. Nat. Hazards 74, 1095–1125.

Chawla, A., Spindler, D.M., Tolman, H.L., 2013. Validation of a thirty year wave hindcast using the climate forecast system reanalysis winds. Ocean Model. 70, 189–206.

Crosby, S.C., O'Reilly, W.C., Guza, R.T., 2016. Modeling long period swell in California: practical boundary conditions from buoy observations and global wave model predictions. J. Atmos. Ocean. Technol. (in press).

Dorrestein, R., 1960. Simplified method for determining refraction coefficients for sea waves. J. Geophys. Res. 65 (2), 637–642.

García-Medina, G., Özkan-Haller, H.T., Ruggiero, P., Oskamp, J., 2013. An inner-shelf wave forecasting system for the U.S. Pacific northwest. Weather Forecast. 28 (3), 681–703.

Hanson, J.L., Tracy, B., Tolman, H., Scott, R., 2009. Pacific hindcast performance of three numerical wave models. J. Atmos. Ocean. Technol. 26, 1614–1633.

Kuik, A.J., van Vledder, G.P., Holthuijsen, L.H., 1988. A method for routine analysis of pitch-and-roll buoy data. J. Phys. Oceanogr. 18, 1020–1034.

LeMehaute, B., Wang, J.D., 1982. Wave spectrum changes on a sloped beach. J. Waterw. Port Coast. Ocean Eng. 108 (WW1), 33–47.

Longuet-Higgins, M.S., 1957. On the transformation of a continuous spectrum by refraction. Proc. Camb. Philos. Soc. 53 (1), 226–229.

Lygre, A., Krogstad, H.E., 1986. Maximum entropy estimation of the directional distribution of ocean wave spectra. J. Phys. Oceanogr. 16 (12), 2052–2060.

Munk, W.H., Miller, G.R., Snodgrass, F.E., Barber, N.F., 1963. Directional recording of swell from distant storms. Philos. Trans. R. Soc. Lond. A 255 (1062), 505–584.

Ochoa, J., Gonzalez, O.E.D., 1990. Pitfalls in the estimation of wind wave spectra by variational principles. Appl. Ocean Res. 12 (4), 180–187.

O'Reilly, W.C., Guza, R.T., 1991. A comparison of spectral refraction and refraction-diffraction wave propagation models. J. Waterw. Port Coast. Ocean Eng. 117 (3), 199–215.

O'Reilly, W.C., Guza, R.T., 1993. A comparison of two spectral wave models in the Southern California Bight. Coast. Eng. 19 (3), 263–282.

O'Reilly, W.C., Herbers, T.H.C., Seymour, R.J., Guza, R.T., 1996. A comparison of directional buoy and fixed platform measurements of Pacific swell. J. Atmos. Ocean. Technol. 13 (1), 231–238.

O'Reilly, W.C., Guza, R.T., 1998. Assimilating coastal wave observations in regional swell predictions. Part I: inverse methods. J. Phys. Oceanogr. 28, 679–691.

Orzech, M., Thornton, E.B., MacMahan, J.H., O'Reilly, W.C., Stanton, T.P., 2010. Alongshore rip migration and sediment transport. Mar. Geol. 271 (3–4), 278–291.

Orzech, M.D., Veeramony, J., Ngodock, H., 2013. A variational assimilation system for nearshore wave modeling. J. Atmos. Ocean. Technol. 30, 953–970.

Panteleev, G., Yaremchuk, M., Rogers, W.E., 2015. Adjoint-free variational data assimilation into a regional wave model. J. Atmos. Ocean. Technol. 32 (7), 1386–1399.

Pierson, W.J., Tuttle, J.J., Wooley, J.A., 1952. The theory of the refraction of a short-crested Gaussian sea surface with application to the northern New Jersey coast. Proceedings of the Third Conference on Coastal Engineering, pp. 86–108.

Rasmussen, L.L., Cornuelle, B.D., Levin, L.A., Largier, J.L., Di Lorenzo, E., 2009. Effects of small-scale features and local wind forcing on tracer dispersion and estimates of population connectivity in a regional scale circulation model. J. Geophys. Res. 114, C01012.

Rogers, W.E., Kaihatu, J.M., Petit, H.A.H., Booij, N., Holthuijsen, L.H., 2002. Diffusion reduction in an arbitrary scale third generation wind wave model. Ocean Eng. 29 (11), 1357–1390.

Rogers, E.W., Kaihatu, J.M., Hsu, L., Jensen, R.E., Dykes, J.D., Holland, K.T., 2007. Forecasting and hindcasting waves with the SWAN model in the Southern California Bight. Coast. Eng. 54 (1), 1–15.

Seymour, R.J., Higgins, A.L., 1978. Continuous estimation of longshore sand transport. ASCE Coast. Zone 78 (3), 2308–2318.

Stockdon, H.F., Holman, R.A., Howd, P.A., Sallenger Jr., A.H., 2006. Empirical parameterization of setup, swash, and runup. Coast. Eng. 53, 573–588.

USACE, 1984. Shore Protection Manual. Coastal Engineering Research Center. Fort Belvoir, Virginia.

Van der Westhuysen, A.J., Padilla-Hernandez, R., Santos, P., Gibbs, A., Gaer, D., Nicolini, T., Tjaden, S., Devaliere, E.M., Tolman, H.L., 2013. Development and validation of the nearshore wave prediction system. Proc. 93rd AMS Annual Meeting. American. Meteorology. Society, Austin TX.